© Indian Academy of Sciences

ACTIVE GALACTIC NUCLEI

Evidence of heavy obscuration in the low-luminosity AGN NGC 4941

ARGHAJIT JANA[1],[*] ⓘ, SACHINDRA NAIK[1] and NEERAJ KUMARI[1],[2]

[1]Department of Astronomy and Astrophysics, Physical Research Laboratory, Ahmedabad 380009, India.
[2]Department of Physics, Indian Institute of Technology, Gandhinagar 382355, India.
*Corresponding author. E-mail: argha@prl.res.in; argha0004@gmail.com

Abstract. We present the results obtained from timing and spectral studies of the highly obscured low luminosity active galactic nucleus NGC 4941 using data obtained from the nuclear spectroscopic telescope array and the Neil Gehrels Swift observatories. We find similar variability in 3–10 keV and 10–60 keV energy ranges with fractional rms variability of $\sim 14\%$. We investigate broad-band spectral properties of the source in 3–150 keV range, using data from NuSTAR and Swift/BAT, with phenomenological slab model and physically motivated MYTORUS model. From the spectral analysis, we find heavy obscuration with global average column density of the obscured material as $3.09^{+1.68}_{-1.01} \times 10^{24}$ cm^{-2}. Evidence of a strong reflection component is observed in the spectrum. We detect a strong iron line with equivalent width of ~ 1 keV. From the slab model, we obtain the exponential cutoff energy as 177^{+92}_{-16} keV. From this, we estimate the Compton cloud properties with the hot electron temperature $kT_{\rm e} = 59^{+31}_{-5}$ keV and the optical depth $\tau = 2.7^{+0.2}_{-1.6}$.

1. Introduction

Active galactic nuclei (AGNs) are believed to be powered by accretion onto the supermassive black holes (Rees 1984) that reside at the center of the galaxies. The accretion disk predominately emits in the UV/optical wavebands (Shakura & Sunyaev 1973). The UV/optical seed photons from the accretion disk undergo inverse Comptonization in the Compton corona producing emission in X-rays (Sunyaev & Titarchuk 1980; Haardt & Maraschi 1991). The emitted X-ray photons can be well approximated with a power-law continuum. A fraction of the emitted X-ray photons is reflected in the surrounding materials, producing Fe K-line complex in ~ 6–8 keV range and a reflection hump in ~ 15–40 keV range (George & Fabian 1991; Matt *et al.* 1991). Additionally, an excess in the soft X-ray (<1 keV), known as soft-excess, is also observed (Singh *et al.* 1985).

Based on the optical observations, the AGNs are broadly classified into two classes depending on the presence or absence of broad emission lines. The broad emission lines (originate in the broad line emitting regions or BLRs) are observed in type-1 AGNs, while it is absent in the type-2 AGNs. The unified model (UM) of AGNs explains different classes of AGNs based on the orientation of viewing angle (Antonucci & Miller 1985; Antonucci 1993). In this model, a dusty torus surrounds the nuclear region at a parsec scale. The type-1 AGNs are observed face-on where the BLRs are visible, while the type-2 AGNs are viewed edge-on where the torus obscures the BLR (Awaki *et al.* 1991). Additionally, the narrow emission lines (originate in narrow line emitting regions or NLRs) are observed in both types of AGNs.

In the X-ray wavebands, the classification of AGNs (obscured or un-obscured) is based on the value of equivalent hydrogen column density ($N_{\rm H}$) along the line of sight which characterizes the obscured material surrounding the AGNs. If the column density $N_{\rm H} < 10^{22}$ cm^{-2}, the AGN is an un-obscured AGN,

whereas if $N_H > 10^{22}$ cm^{-2}, the AGN is classified as an obscured AGN. The obscured AGNs can be further classified as Compton-thin or Compton-thick (CT). If the column density $N_H > 10^{24}$ cm^{-2}, the AGN is classified as Compton-thick AGN (Hickox & Alexander 2018).

Recently, a new sub-class of AGNs has emerged, known as changing-look AGNs (CLAGNs). In optical changing-look events (hereafter, changing-state (CS) event), the type-1 (or type 1.2/1.5) AGNs transit to type-2 (or type 1.8/1.9) and vice versa with the disappearance or appearance of the broad emission lines. Several nearby galaxies, such as NGC 1566 (Parker *et al.* 2019), NGC 3516 (Ilić *et al.* 2020), Mrk 590 (Denney *et al.* 2014), NGC 2617 (Shappee *et al.* 2014), Mrk 1018 (Noda & Done 2018) have been found to show such peculiar behavior. A different type of changing-look events have been observed in the X-ray wavebands, with an AGN switching between Compton-thin ($N_H < 10^{24}$ cm^{-2}) and Compton-thick (CT; $N_H > 10^{24}$ cm^{-2}) states (Risaliti *et al.* 2002; Matt *et al.* 2003). The X-ray CL events (hereafter, changing-obscuration (CO) event) have been observed in many AGNs, namely IC 751 (Ricci *et al.* 2016), NGC 4507 (Braito *et al.* 2013), NGC 6300 (Jana *et al.* 2020).

Low luminosity AGNs (LLAGNs; bolometric luminosity $L_{bol} < 10^{43}$ erg s^{-1}) holds key to understand the changing-state events. Many changing-state AGNs are observed to remain in the low-luminosity state over decades before showing a CS event. Recently, NGC 1566 showed an outburst in June 2018 after remaining in the low luminosity state for over a decade (Jana *et al.* 2021). During the outburst, the optical, UV, and X-ray flux increased by $\sim$25–30 times compared to the low luminosity state with the reappearance of broad emission lines (Oknyansky *et al.* 2020). Similar behavior is also observed in NGC 3516 (Ilić *et al.* 2020). Thus, it is essential to study the accretion properties of low-luminosity AGNs.

NGC 4941 is classified as a Seyfert 2 galaxy (Véron-Cetty & Véron 2006) with a morphological class of Sa (Fisher & Drory 2008). Over the past years, NGC 4941 was observed with several X-ray observatories, such as ASCA (Terashima *et al.* 2002), BeppoSAX (Maiolino *et al.* 1998), Chandra (Bottacini *et al.* 2012), Suzaku (Kawamuro *et al.* 2013) and NuSTAR (Georgantopoulos & Akylas 2019; García-Burillo *et al.* 2021). The ASCA, BeppoSAX, Suzaku and NuSTAR observations revealed a heavily obscured nucleus with line of sight column density

$N_H > 10^{23}$ cm^{-2} and a strong Fe K_α emission line in the spectrum. The mass of the black hole in NGC 4941 is reported to be $\sim 10^{6.9} M_\odot$ (Asmus *et al.* 2011). While investigating the obscuration properties of Swift/BAT AGNs, several authors used NuSTAR observations of Swift/BAT AGNs, and carried out systematic spectral studies to understand the nature of the torus of the AGN sample (Georgantopoulos & Akylas 2019; Baloković *et al.* 2020; García-Burillo *et al.* 2021; Zhao *et al.* 2021). Though the NuSTAR observation of NGC 4941 on 19 January 2016 was used in above studies, a detailed investigation of the source properties was not carried out. Considering this, we performed spectral and timing studies of NGC 4941 in broad energy range using data from NuSTAR (on 19 January 2016) and Swift/BAT observations.

The paper is organized as follows. In Section 2, we describe the observation and data extraction process. We present the results obtained from the timing and spectral analysis in Section 3. In Section 4, we discuss our findings. The summary of the work is presented in Section 5.

2. Observation and data extraction

NGC 4941 was observed with NuSTAR on 19 January 2016 for an exposure of $\sim$21 ks. NuSTAR is a hard X-ray focusing telescope consisting of two identical modules: FPMA and FPMB (Harrison *et al.* 2013). We reprocessed the raw data with the NuSTAR data analysis software (NuSTARDAS, version 1.4.1). Cleaned event files were generated and calibrated using the standard filtering criteria in the nupipeline task and the latest calibration data files available in the NuSTAR calibration database (CALDB).[1] We extracted the source and background products considering circular regions with radii 60 arc-sec and 90 arc-sec, respectively. The spectra and light curves were extracted using the nuproduct task. The light curves were binned at 500 s. To improve the S/N, we co-added FPMA and FPMB spectra using ADDAS-CASPEC task. We re-binned the spectra with 20 counts per bin by using the grppha task. We analysed NuSTAR spectrum in 3–60 keV energy range. We also included the spectrum of the source from Swift/BAT in 14–150 keV range, obtained from the 105-month BAT survey (Oh *et al.* 2018).[2]

---

[1]http://heasarc.gsfc.nasa.gov/FTP/caldb/data/nustar/fpm/.

[2]https://swift.gsfc.nasa.gov/results/bs105mon/653.

3. Results

We studied NGC 4941 using the data obtained from the NuSTAR and Swift/BAT in a combined energy range of 3–150 keV. In our study, we used following cosmological parameters: $H_0 = 70$ km s^{-1} Mpc^{-1}, $\Lambda_0 = 0.73$ and $\Omega_M = 0.27$ (Bennett *et al.* 2003).

3.1 *Timing properties*

To study time variability in the source, we generated light curves in 3–10 keV and 10–60 keV energy ranges with a time-resolution of 500 s from NuSTAR data. Figure 1 shows the light curves in 3–10 keV and 10–60 keV energy ranges in the top and middle panels, respectively. In the bottom panel of Figure 1, we show the variation of hardness ratio (HR) which is defined as the ratio between the count rates in 10–60 keV and 3–10 keV bands. To study the variability, we calculated the fractional rms amplitude (F_{var}) for the light curves in different energy ranges (Vaughan *et al.* 2003). Both energy bands showed similar variabilities with $F_{var} = 14.4 \pm 4.8\%$ and $14.5 \pm 7.4\%$ in 3–10 keV and 10–60 keV ranges, respectively.

3.2 *Spectral properties*

We carried out spectral analysis of NGC 4941 using HEASEARC's spectral analysis package XSPECv12.10[3] (Arnaud 1996). In our spectral analysis, we used data in 3–60 keV and 14–150 keV ranges from the NuSTAR and Swift/BAT observations, respectively, to get a broad-band coverage of 3–150 keV energy range. All the errors are quoted at 1.6σ level (90% confidence).

3.2.1 *Slab model*
We started our analysis with phenomenological models (hereafter slab model) POWERLAW and PEXRAV (Magdziarz *et al.* 1998). The slab model consists of an absorbed power-law continuum with an exponential cut-off, reflection from cold materials and Fe *K*-line. Additionally, we also included a scattered emission which is often observed in the Compton thin sources (Turner *et al.* 1997). We did not include any component for the soft-excess as we study in the energy range of 3–150 keV. The cold reflection component was modeled with PEXRAV component. PEXRAV describes the reflection
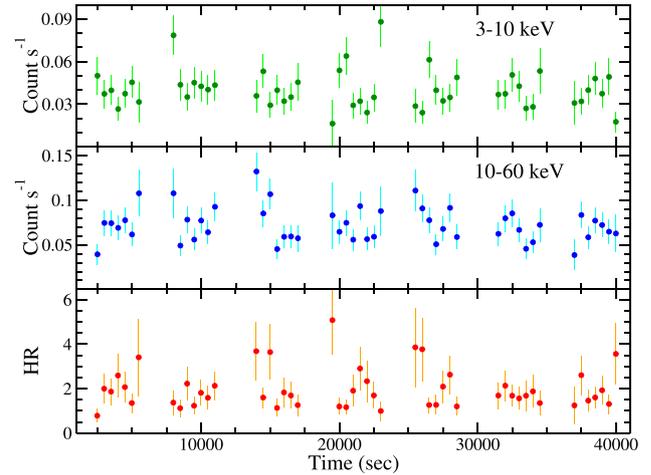
---

[3]https://heasarc.gsfc.nasa.gov/xanadu/xspec/.

Figure 1. Light curves of NGC 4941 in 3–10 keV (top panel) and 10–60 keV (middle panel) ranges, obtained from NuSTAR observation, are shown. The bottom panel shows the variation of the hardness ratio.

from a cold semi-infinite slab. The power-law photon index, cut-off energy and normalization were tied up with the primary continuum. We set the reflection fraction (R_{refl}) to a negative value, thus, PEXRAV only considered as the reflection component. We fixed the abundances to the Solar value and inclination angle to 60°. Thus, the only free parameter in PEXRAV was the reflection fraction (R_{refl}). We modeled the scattered emission with a power-law with exponential cut-off and tied the parameters with the primary emission. The scattering fraction (f_{Scat}) was estimated by using a multiplicative constant with the scattering emission. Our complete model can be written in XSPEC as:

CONSTANT1 * PHABS1 * (ZPHABS * CABS * ZCUTOFF
    + PEXRAV + ZGAUSS + CONSTANT2 * ZCUTOFF).

Here, CONSTANT1 and CONSTANT2 are the cross-normalization between NuSTAR and BAT, and scattered fraction, respectively. PHABS1 represents the Galactic absorption in the direction of the source which we fixed at the Galactic value of 2.25×10^{20} cm^{-2} (HI4PI Collaboration *et al.* 2016). The ZPHABS and CABS components represent absorptions due to the line of sight column density and Compton scattering, respectively. The column densities of these two models were tied together. During our analysis, we fixed the line width of the Gaussian component at 0.1 keV.

The spectral analysis with the slab model gave us a good fit with a $\chi^2 = 164$ for 161 degrees of freedom (dof). We obtained the photon index $\Gamma = 1.47 \pm 0.05$, cut-off energy, $E_{cut} = 177^{+92}_{-16}$ and reflection fraction $R_{refl} < 0.89$. The Fe K_α line was detected at 6.33

$\pm$ 0.05 keV with equivalent width EW $= 0.71^{+0.03}_{-0.01}$ keV. We also found the source in the Compton-thin state with the line of sight column density $N_H = (7.5 \pm 0.3) \times 10^{23}$ cm^{-2}. The best-fit parameters obtained from our spectral fitting are presented in Table 1. Figure 2 shows the best-fitted spectrum with slab model in the top left panel. Corresponding residuals are shown in the bottom left panel of the figure. The right panel of Figure 2 shows the unfolded spectrum. The black, blue, red, green and magenta lines represent the total, primary continuum, reprocessed emission, Fe K_α line, and scattered emission, respectively. Figure 3 shows the confidence contour between the photon index (Γ) and cut-off energy (E_{cut}).

3.2.2 *Torus model* The PEXRAV model does not consider the complex structure of the torus. Hence, the slab model does not give us complete information on the reprocessed emission or obscured materials. Various torus-based models have been developed considering the complex structure and geometry of the torus and estimated the reprocessed emission self-consistently (Murphy & Yaqoob 2009; Brightman & Nandra 2011; Paltani & Ricci 2017; Tanimoto *et al.* 2019). Here, we studied NGC 4941 with physically motivated torus-based model MYTORUS (Murphy & Yaqoob 2009; Yaqoob 2012)[4].

The MYTORUS model considers a dusty absorbing torus with uniform density surrounding the nucleus with a fixed covering factor 0.5, i.e., half-opening angle of 60°. The MYTORUS model has three components: absorbed primary emission or zeroth

ordered component (MYTZ), reprocessed emission (MYTS) and an iron fluorescent line emission (MYTL; Fe K_α and Fe K_β). One can use the MYTORUS model in two configurations: coupled and decoupled. The

Table 1. Spectral analysis results.

Parameters	Slab	MYTorus
C_{BAT}	1.12 ± 0.22	$1.11^{+0.34}_{-0.29}$
N_H^{los} (10^{24} cm^{-2})	$0.75^{+0.33}_{-0.29}$	0.76 ± 0.09
N_H^{tor} (10^{24} cm^{-2})	–	$3.09^{+1.68}_{-1.01}$
Photon index Γ	1.47 ± 0.05	1.71 ± 0.10
E_{cut} (keV)	177^{+92}_{-16}	–
N_{PL}	6.08 ± 0.12	6.73 ± 0.15
R_{refl}	<0.89	–
A_S	–	3.15 ± 0.32
f_{Scat} (10^{-2})	$8.04^{+0.35}_{-0.78}$	$9.32^{+0.35}_{-0.41}$
Fe K_α EW (keV)	$0.71^{+0.03}_{-0.01}$	$1.03^{+0.07}_{-0.13}$
χ^2/dof	165/161	165/162
F^{obs}_{2-10}	7.52 ± 0.08	7.54 ± 0.09
L^{int}_{2-10}	2.12 ± 0.61	2.13 ± 0.66
L_{bol}	3.18 ± 0.92	3.19 ± 0.99

All the errors are quoted at 90% confidence (1.6σ) level. C_{BAT} is cross-normalization factor of BAT and NuSTAR. N_H^{los} and N_H^{tor} are the line of sight column density and averaged global column density of the torus, respectively. N_{PL} (power-law normalization) is in the unit of 10^{-4} ph cm^{-2} s^{-1}. F^{obs}_{2-10} (observed flux in 2–10 keV range) is in unit of 10^{-13} ergs cm^{-2} s^{-1}. L^{int}_{2-10} (intrinsic luminosity in 2–10 keV range) is in unit of 10^{41} ergs s^{-1}. L_{bol} (bolometric luminosity) is in unit of 10^{42} ergs s^{-1}.
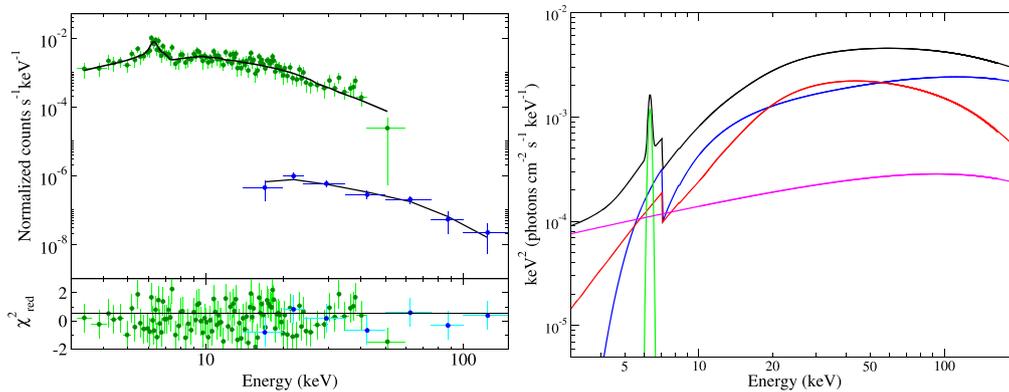

Figure 2. Left side: upper panel – slab model fitted spectrum (black solid line). Green and blue circles represent the NuSTAR and Swift/BAT data, respectively. Bottom panel – residuals in terms of data–model/error. Right side: the unfolded spectrum. The black, blue, red, green and magenta lines represent the total, primary continuum, reprocessed emission, Fe K_α line and scattered emission, respectively.
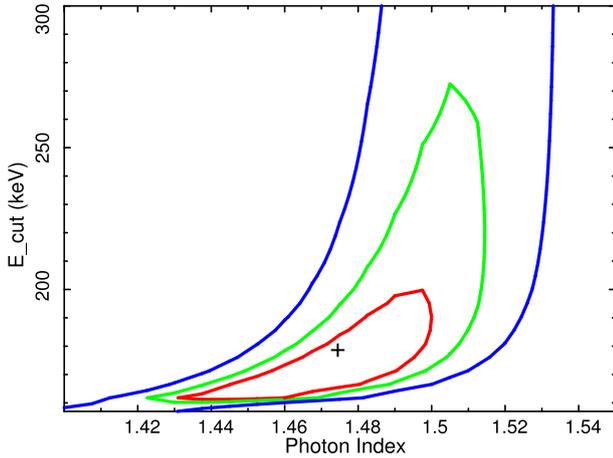
[4]https://mytorus.com.

Figure 3. Confidence contours between the photon index (Γ) and cut-off energy (E_{cut}).

coupled configuration considers a uniform torus, while the decoupled configuration describes a clumpy or patchy torus. Many studies suggest that the torus is not uniform, rather made up of clumps of gas as opposed to what the UM had suggested (Krolik & Begelman 1988; Laor & Draine 1993; Hönig & Beckert 2007; Hönig *et al.* 2012; Nenkova *et al.* 2008a,b). Thus, we applied the decoupled configuration of the MYTORUS model to the combined spectra of NGC 4941. The model is represented as follows:

CONSTANT1 * PHABS1 * (POWERLAW * MYTZ
    + A_S * MYTS + A_L * GSMOOTH * MYTL
    + CONSTANT2 * POWERLAW).

Here, the photon index (Γ) and normalization of all four components are tied together. The inclination angle becomes a dummy parameter in this configuration (Yaqoob 2012). Hence, the inclination of the MYTZ was set to 90°, while the inclination of MYTS and MYTL were set to 0°. The column density of the MYTZ component represents the line of sight column density (N_H^{los}). The column densities of the MYTS and MYTL components were tied together. This column density represents the averaged global column density of the obscured materials (N_H^{tor}). The MYTS component represents the reprocessed emission from the backside of the torus. As recommended, the relative normalization of the reflected (A_S) and line emission (A_L) components were tied, i.e., $A_S = A_L$. The last term represents the scattered primary emission as in the slab model.

The spectral fitting with this model gave us a good fit with $\chi^2 = 165$ for 162 dof. The line of sight column density and averaged column density of the obscured

material were estimated to be $N_H^{los} = (0.76 \pm 0.09) \times 10^{24}$ cm^{-2} and $N_H^{tor} = 3.09_{-1.01}^{+1.68} \times 10^{24}$ cm^{-2}, respectively. The photon index ($\Gamma = 1.71 \pm 0.10$) was found to be flatter compared to the slab model. The relative normalization of the reprocess emission was obtained to be $A_S = 3.15 \pm 0.32$.

As Fe K_α and Fe K_β lines are calculated self-consistently in MYTORUS model, the EW cannot be estimated in a straightforward way. The EW is calculated in the observed frame by taking the ratio of the total continuum flux to the line flux in 6.08–6.72 keV range ($0.95E_{K_\alpha}$–$1.05E_{K_\alpha}$). Then EW is calculated in the rest frame energy by multiplying with $(1 + z)$. A strong iron line was also observed with MYTORUS model with EW $= 1.03_{-0.13}^{+0.07}$ keV. The FWHM of Fe K_α line was obtained from the convolution model GSMOOTH, with FWHM $= 117.7\sigma_L$ (eV) km s^{-1}. We found the FWHM of the line as <4900 km s^{-1}. The results obtained from a detailed spectral analysis of the decoupled configuration of MYTORUS model is presented in Table 1. The best-fitted spectrum with MYTORUS model and corresponding residuals are shown in the top and bottom panels of the left side of Figure 4. The panel in the right side of Figure 4 shows the unfolded spectrum, fitted with the decoupled configuration of MYTORUS model. The black, blue, red, green and magenta lines in the panel represent the total, primary continuum, reprocessed emission, Fe K_α and Fe K_β lines, and scattered emission, respectively. Figure 5 shows the confidence contours between the line of sight column density (N_H^{los}) and averaged global column density of the obscured material (N_H^{tor}).

4. Discussion

In the present work, we studied the timing and spectra properties of low-luminosity highly obscured AGN NGC 4941 using combined data from NuSTAR and Swift/BAT in 3–150 keV range in detail. The broad-band investigation allowed us to understand the properties of the nucleus and obscuration of the AGN in the present study.

We observed similar variability in 3–10 keV and 10–60 keV energy ranges with $F_{var} \sim 14\%$. The observed variability is found to be comparable to other Seyfert galaxies (Hernández-García *et al.* 2015). In general, the primary photons and reprocessed photons dominate in 3–10 keV and 10–60 keV energy ranges, respectively. Therefore, the variability is expected to be different in different energy bands. However, in
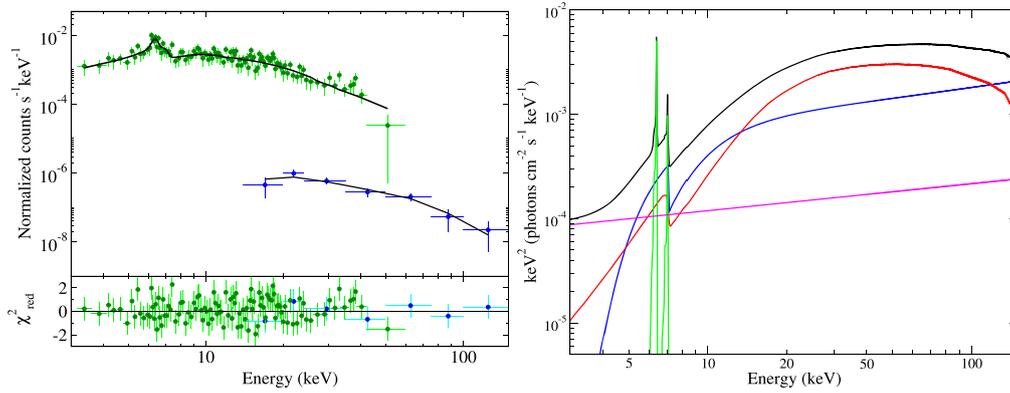
Figure 4. Left side: upped panel – MYTorus model fitted spectrum (black solid line) is shown. Green and blue circles represent the NuSTAR and Swift/BAT data, respectively. Bottom panel – residuals in terms of data–model/error. Right side: the unfolded spectrum is shown. The black, blue, red, green and magenta lines represent the total, primary continuum, reprocessed emission, Fe K_α and Fe K_β lines, and scattered emission, respectively.
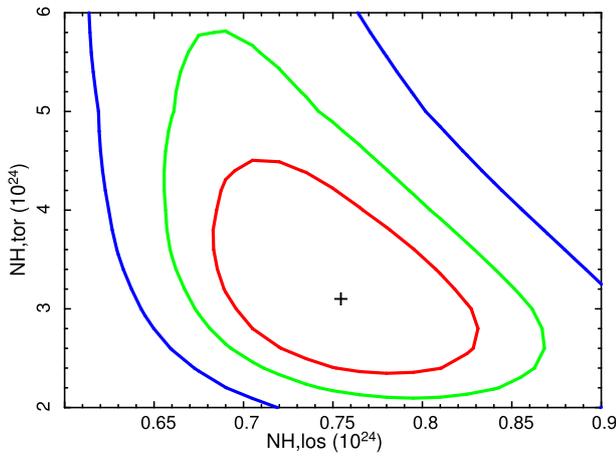

Figure 5. Confidence contours between N_H^{los} and N_H^{tor}.

NGC 4941, we observe a similar contribution of the primary and reprocessed emission in 3–10 keV and 10–60 keV energy bands. The ratios between the primary and reprocessed flux in 3–10 keV and 10–60 keV energy bands are estimated to be F_{PL}/F_{refl} ~ 1.01 and ~ 0.98, respectively, from the slab model. This is the probable reason for similar variabilities in the above energy bands.

For our study, we used the phenomenological slab model and physically motivated MYTORUS model. Although both models gave us similar statistics, a clear discrepancy of the derived parameters is visible. It is clear from Figures 2 and 4 that the reprocessed emission is greater in the MYTORUS model compared to that in the slab model. This can be seen from the derived parameters A_S and R_{refl}. Although A_S is not the same as R_{refl}, it can be used as a proxy of reflection fraction. From our spectral analysis, we

obtained $R_{refl} < 0.89$ and $A_S = 3.15 \pm 0.32$ from the slab model and MYTORUS model, respectively. The slab model indicates that the continuum emission dominates while the MYTORUS model indicates the opposite. This discrepancy arises due to different treatment of the reprocessed emission by a different model. The slab model does not consider the complex structure of the torus. Hence, this model may not calculate the reprocessing component correctly. On the other hand, MYTORUS considers the complex structure of the torus. Therefore, it describes the reprocessed emission more accurately. Different treatments of the reprocessed emission affects the spectral shape, as the photon index was flatter in the MYTORUS model.

The relative normalization obtained from the MYTORUS model was $A_S = 3.15 \pm 0.32$. The deviation from unity indicates that either the reprocessed emission was delayed or the torus covering factor deviated from 0.5 or multiple absorbers with different column densities exist along the line of sight (Yaqoob 2012).

Zhao *et al.* (2021) studied NGC 4941 with BORUS model (Baloković *et al.* 2018) and estimated the line of sight column density and torus column density as $N_H^{los} = 9.5^{+9.5}_{-3.5} \times 10^{23}$ cm^{-2} and $N_H^{tor} = 3.2^{+5.5}_{-2.5} \times 10^{24}$ cm^{-2}, respectively. García-Burillo *et al.* (2021) also studied the source assuming the torus covering factor as 1 and found the line of sight column density and torus column density as $N_H^{los} = 4.2 \pm 1.1 \times 10^{23}$ cm^{-2} and $N_H^{tor} = 1.4 \pm 0.3 \times 10^{24}$ cm^{-2}, respectively. Georgantopoulos & Akylas (2019) applied a different configuration of MYTORUS model to the same set of NuSTAR and BAT data and estimated the equatorial

column density $N_H^{Eq} = 1.2_{-0.4}^{+0.9} \times 10^{24}$ cm^{-2}. In their analysis, they used COMPTT model (Titarchuk 1994) as the primary emission. However, we used POWERLAW as the primary emission in our analysis. We obtained the line of sight column density as $N_H^{los} = (0.76 \pm 0.09) \times 10^{24}$ cm^{-2}. The Suzaku observation in June 2012 reported the line of sight column density as $N_H^{los} = (0.73 \pm 0.19) \times 10^{24}$ cm^{-2}, which is consistent with our result (Kawamuro *et al.* 2013). From the previous observation of NGC 4941, a variable N_H^{los} was observed though the timescale of variability could not be determined. In July 1996, ASCA observed the source in the CT state with $N_H^{los} = (0.99 \pm 0.12) \times 10^{24}$ cm^{-2} (Maiolino *et al.* 1998). BeppoSAX observed the source six months later and found the source in Compton-thin state with $N_H^{los} = 0.45_{-0.14}^{+0.24} \times 10^{24}$ cm^{-2} (Terashima *et al.* 2002). From the past observations, it is also clear that NGC 4941 shows variability of N_H in months timescale although the variability in shorter timescales cannot be ruled out. The spectral analysis with the MYTORUS model also revealed the averaged global column density of the obscured medium as $N_H^{tor} = 3.09_{-1.01}^{+1.68} \times 10^{24}$ cm^{-2} (present work).

In our study, we found a strong Fe K_α line with EW $= 1.03_{-0.13}^{+0.07}$ keV. A strong signature of Fe K_α line was also observed in past. The ASCA and BeppoSAX observations reported the EW of Fe K_α line as 0.57 ± 0.23 keV and 1.6 ± 0.8 keV, respectively (Maiolino *et al.* 1998; Terashima *et al.* 2002). In contrast, a comparatively weak iron line with EW $= 0.38 \pm 0.08$ keV was detected in the Suzaku data (Kawamuro *et al.* 2013). Kawamuro *et al.* (2013) found that the flux of the iron K_α line was consistent across the observations. The Fe K_α line flux was estimated to be 1.0 ± 0.4, 1.2 ± 0.6 and $0.67 \pm 0.12 \times 10^{-5}$ photons cm^{-2} s^{-1} from the ASCA, BeppoSAX and Suzaku observations, respectively (Terashima *et al.* 2002; Cardamone *et al.* 2007; Kawamuro *et al.* 2013). In our analysis, the Fe K_α line flux is estimated to be $0.76 \pm 0.18 \times 10^{-6}$ photons cm^{-2} s^{-1} which is consistent with the previous observations. The consistent iron line flux indicated that the reflection flux originating at the torus, therefore, is constant over the years (Kawamuro *et al.* 2013).

We estimated the intrinsic luminosity of the source in 2–10 keV energy range as $L_{2-10}^{int} = 2.13 \times 10^{41}$ ergs s^{-1}. Considering the bolometric correction factor $\kappa_{2-10} = 20$ (Vasudevan & Fabian 2009), we obtained

the bolometric luminosity $L_{bol} = (4.26 \pm 1.32) \times 10^{42}$ ergs s^{-1}. This indicates that the Eddington ratio $\lambda_{Edd} = L/L_{Edd} = 0.0041 \pm 0.0013$. The observed Eddington ratio is consistent with the other Seyfert 2 galaxies (Wu & Liu 2004). The 2–10 keV intrinsic luminosity of the source, estimated from the Suzaku observation which was carried out ~ 3.5 years prior to the NuSTAR observation, was 1.98×10^{41} ergs s^{-1}. This suggests a $\sim 10\%$ change in the mass accretion rate in the source over ~ 3.5 years.

The X-ray emitting Compton corona is characterized by the hot electron temperature (kT_e) and the optical depth (τ). One can make crude approximation of kT_e and τ without detailed modeling if the photon index (Γ) and cut-off energy (E_{cut}) are known. In general, $E_{cut} = 2 - 3 kT_e$ (Petrucci *et al.* 2001). Specifically,

$$\begin{aligned} E_{cut} &= 2 kT_e & \text{for} \quad \tau \leq 1, \\ &= (1 + \tau) kT_e & \text{for} \quad 1 < \tau < 2, \\ &= 3 kT_e & \text{for} \quad \tau \geq 2. \end{aligned}$$

From our spectral analysis with the slab model, we found that the cut-off energy of the source is $E_{cut} = 177_{-16}^{+92}$ keV. From this, the hot electron temperature is estimated to be either 88_{-8}^{+46} keV or 59_{-5}^{+31} keV, or between these. One can calculate the optical depth from the following equation (Titarchuk 1994; Zdziarski *et al.* 1996),

$$\tau \approx \sqrt{\frac{9}{4} + \frac{m_e c^2}{kT_e} \frac{3}{(\Gamma - 1)(\Gamma + 2)}} - \frac{3}{2}.$$

Using this relation, we obtained $\tau \sim 2$ (for $kT_e \sim 88$ keV) or $\tau \sim 2.7$ (for $kT_e \sim 59$ keV). From this, it is clear that the the hot electron temperature, $kT_e = 59_{-5}^{+46}$ keV and the optical depth $\tau = 2.7_{-1.6}^{+0.2}$. Baloković *et al.* (2020) also estimated the cutoff energy of the source as $E_{cut} = 110_{-60}^{+u}$ keV. They calculated the optical depth of the corona as $\tau = 3.6$. Though the value of τ is marginally different from our estimation, the cut-off energy is consistent with our measurement.

We also tried to estimate the Compton corona temperature and the optical depth from detailed spectral modeling. We replaced the POWERLAW in the slab model with COMPTT model. We carried out spectral fitting for spherical and slab coronae. We obtained $kT_e = 67_{-54}^{+145}$ keV and $\tau = 4.18_{-3.65}^{+4.28}$ for the spherical corona and $kT_e = 74_{-59}^{+136}$ keV and $\tau = 1.81_{-1.26}^{+2.40}$ for the slab corona. Although, the COMPTT model yielded a higher uncertainty in the obtained values, it is

consistent with the crude approximation. Georgantopoulos & Akylas (2019) also estimated the Compton corona temperature from the fitting with MYTORUS model as $kT_e = 47^{+216}_{-34}$ keV. Our finding is consistent with this.

5. Conclusion and summary

We studied NGC 4941 using the combined data of NuSTAR and Swift/BAT. NGC 4941 is reported to be a low luminosity AGN with $L_{bol} < 10^{43}$ ergs s^{-1}. From the previous X-ray studies, NGC 4941 is observed to be a highly obscured AGN. Following are the findings from our work:

1. NGC 4941 shows similar variability in 3–10 keV and 10–60 keV energy ranges with $F_{var} \sim 14\%$.
2. We obtained the line of sight column density $N_H^{los} = (0.76 \pm 0.09) \times 10^{24}$ cm^{-2} from the spectral analysis with MYTORUS model. The slab model also showed similar value. The averaged global torus density is found to be $N_H^{tor} = 3.09^{+1.68}_{-1.01} \times 10^{24}$ cm^{-2} suggesting as Compton-thick.
3. We find evidence of strong reflection in the source from both slab and MYTORUS models. A deviation of relative normalization (A_S) from unity indicates a delayed reprocessed emission.
4. The iron K-line emission is observed to be strong with EW = $1.03^{+0.07}_{-0.13}$ keV.
5. The bolometric luminosity is estimated to be $L_{bol} = (4.26 \pm 1.32) \times 10^{42}$ ergs s^{-1}. We obtain the Eddington ratio of the source as $\lambda_{Edd} = 0.0041 \pm 0.0013$.
6. The cut-off energy of the source is found to be as $E_{cut} = 177^{+92}_{-16}$ keV. From this, we estimate the hot electron temperature and optical depth of the Compton cloud as $kT_e = 59^{+31}_{-5}$ keV and $\tau = 2.7^{+0.2}_{-1.6}$.

References

Antonucci R. 1993, ARA&A, 31, 473

Antonucci R. R. J., Miller J. S. 1985, ApJ, 297, 621

Arnaud K. A. 1996, in eds Jacoby G. H., Barnes J., Astronomical Society of the Pacific Conference Series, Vol. 101, Astronomical Data Analysis Software and Systems V, 17

Asmus D., Gandhi P., Smette A., Hönig S. F., Duschl W. J. 2011, A&A, 536, A36

Awaki H., Kunieda H., Tawara Y., Koyama K. 1991, 43, L37

Baloković M., Brightman M., Harrison F. A., *et al.* 2018, ApJ, 854, 42

Baloković M., Harrison F. A., Madejski G., *et al.* 2020, ApJ, 905, 41

Bennett C. L., Halpern M., Hinshaw G., *et al.* 2003, ApJS, 148, 1

Bottacini E., Ajello M., Greiner J. 2012, ApJS, 201, 34

Braito V., Ballo L., Reeves J. N., *et al.* 2013, MNRAS, 428, 2516

Brightman M., Nandra K. 2011, MNRAS, 413, 1206

Cardamone C. N., Moran E. C., Kay L. E. 2007, AJ, 134, 1263

Denney K. D., De Rosa G., Croxall K., *et al.* 2014, ApJ, 796, 134

Fisher D. B., Drory N. 2008, AJ, 136, 773

García-Burillo S., Alonso-Herrero A., Ramos Almeida C., *et al.* 2021, A&A, 652, A98

Georgantopoulos I., Akylas A. 2019, A&A, 621, A28

George I. M., Fabian A. C. 1991, MNRAS, 249, 352

Haardt F., Maraschi L. 1991, ApJL, 380, L51

Harrison F. A., Craig W. W., Christensen F. E., *et al.* 2013, ApJ, 770, 103

Hernández-García L., Masegosa J., González-Martín O., Márquez I. 2015, A&A, 579, A90

HI4PI Collaboration, Ben Bekhti N., Flöer L., *et al.* 2016, A&A, 594, A116

Hickox R. C., Alexander D. M. 2018, ARA&A, 56, 625

Hönig S. F., Beckert T. 2007, MNRAS, 380, 1172

Hönig S. F., Kishimoto M., Antonucci R., *et al.* 2012, ApJ, 755, 149

Ilić D., Oknyansky V., Popović L. Č., *et al.* 2020, A&A, 638, A13

Jana A., Chatterjee A., Kumari N., *et al.* 2020, MNRAS, 499, 5396

Jana A., Kumari N., Nandi P., *et al.* 2021, MNRAS, 507, 687

Kawamuro T., Ueda Y., Tazaki F., Terashima Y. 2013, ApJ, 770, 157

Krolik J. H., Begelman M. C. 1988, ApJ, 329, 702

Laor A., Draine B. T. 1993, ApJ, 402, 441

Magdziarz P., Blaes O. M., Zdziarski A. A., Johnson W. N., Smith D. A. 1998, MNRAS, 301, 179

Maiolino R., Salvati M., Bassani L., *et al.* 1998, A&A, 338, 781

Matt G., Perola G. C., Piro L. 1991, A&A, 247, 25

Murphy K. D., Yaqoob T. 2009, MNRAS, 397, 1549

Nenkova M., Sirocky M. M., Ivezić Ž., Elitzur M. 2008a, ApJ, 685, 147

Nenkova M., Sirocky M. M., Nikutta R., Ivezić Ž., Elitzur M. 2008b, ApJ, 685, 160

Noda H., Done C. 2018, MNRAS, 480, 3898

Oh K., Koss M., Markwardt C. B., *et al.* 2018, ApJS, 235, 4

Oknyansky V. L., Winkler H., Tsygankov S. S., *et al.* 2020, MNRAS, 498, 718

Paltani S., Ricci C. 2017, A&A, 607, A31

Parker M. L., Schartel N., Grupe D., *et al.* 2019, MNRAS, 483, L88

Petrucci P. O., Haardt F., Maraschi L., *et al.* 2001, ApJ, 556, 716

Rees M. J. 1984, ARA&A, 22, 471

Ricci C., Bauer F. E., Arevalo P., *et al.* 2016, ApJ, 820, 5

Shakura N. I., Sunyaev R. A. 1973, A&A, 500, 33

Shappee B. J., Prieto J. L., Grupe D., *et al.* 2014, ApJ, 788, 48

Singh K. P., Garmire G. P., Nousek J. 1985, ApJ, 297, 633

Sunyaev R. A., Titarchuk L. G. 1980, A&A, 500, 167

Tanimoto A., Ueda Y., Odaka H., *et al.* 2019, ApJ, 877, 95

Terashima Y., Iyomoto N., Ho L. C., Ptak A. F. 2002, ApJS, 139, 1

Titarchuk L. 1994, ApJ, 434, 570

Turner T. J., George I. M., Nandra K., Mushotzky R. F. 1997, ApJS, 113, 23

Vasudevan R. V., Fabian A. C. 2009, MNRAS, 392, 1124

Vaughan S., Edelson R., Warwick R. S., Uttley P. 2003, MNRAS, 345, 1271

Véron-Cetty M. P., Véron P. 2006, A&A, 455, 773

Wu X.-B., Liu F. K. 2004, ApJ, 614, 91

Yaqoob T. 2012, MNRAS, 423, 3360

Zdziarski A. A., Johnson W. N., Magdziarz P. 1996, MNRAS, 283, 193

Zhao X., Marchesi S., Ajello M., *et al.* 2021, A&A, 650, A57